












The discovery of a $z = 0.7092$ OH megamaser with the MIGHTEE survey

Matt J. Jarvis ^{1,2}★ Ian Heywood,^{1,3,4} Sophie M. Jewell,^{1,5} Roger P. Deane ^{6,7} H.-R. Klöckner,⁸ Anastasia A. Ponomareva ¹ Natasha Maddox ⁹ Andrew J. Baker,^{2,10} Alessandro Bianchetti,^{11,12} Kelley M. Hess,¹³ Hayley Roberts,^{14,15} Giulia Rodighiero ^{11,12} Ilaria Ruffa ¹⁶ Francesco Sinigaglia,^{11,12,17} Rohan G. Varadaraj ¹ Imogen H. Whittam ¹ Elizabeth A. K. Adams,^{18,19} Maarten Baes ²⁰ Eric J. Murphy,²¹ Hengxing Pan ¹ and Mattia Vaccari ^{22,23,24}

Affiliations are listed at the end of the paper

Accepted 2023 December 6. Received 2023 December 6; in original form 2023 November 5

ABSTRACT

We present the discovery of the most distant OH megamaser (OHM) to be observed in the main lines, using data from the MeerKAT International Giga-Hertz Tiered Extragalactic Exploration (MIGHTEE) survey. At a newly measured redshift of $z = 0.7092$, the system has strong emission in both the 1665 MHz ($L \approx 2500 L_{\odot}$) and 1667 MHz ($L \approx 4.5 \times 10^4 L_{\odot}$) transitions, with both narrow and broad components. We interpret the broad line as a high-velocity-dispersion component of the 1667 MHz transition, with velocity $v \sim 330 \text{ km s}^{-1}$ with respect to the systemic velocity. The host galaxy has a stellar mass of $M_{\star} = 2.95 \times 10^{10} M_{\odot}$ and a star formation rate of $\text{SFR} = 371 M_{\odot} \text{ yr}^{-1}$, placing it ~ 1.5 dex above the main sequence for star-forming galaxies at this redshift, and can be classified as an ultraluminous infrared galaxy. Alongside the optical imaging data, which exhibit evidence for a tidal tail, this suggests that the OHM arises from a system that is currently undergoing a merger, which is stimulating star formation and providing the necessary conditions for pumping the OH molecule to saturation. The OHM is likely to be lensed, with a magnification factor of ~ 2.5 , and perhaps more if the maser emitting region is compact and suitably offset relative to the centroid of its host galaxy's optical light. This discovery demonstrates that spectral line mapping with the new generation of radio interferometers may provide important information on the cosmic merger history of galaxies.

Key words: masers – ISM: molecules – galaxies: ISM – galaxies: starburst.

1 INTRODUCTION

Hydroxyl masers were discovered over five decades ago, with the majority of early detections coming from compact H II regions in our own Galaxy (Weaver et al. 1965). Perkins, Gold & Salpeter (1966) were the first to interpret these lines as maser emission, which provided an explanation for the high brightness temperature, polarization properties, and the line ratios. The following year, Wilson & Barrett (1968) discovered OH emission from four infrared stars, although many more did not exhibit detectable OH emission. Heiles (1968) also detected OH emission from interstellar dust clouds, suggesting that OH emission arose from regions with a large preponderance of infrared emission. As observations of the sky at radio wavelengths became more widespread, OH emission was discovered in external galaxies (e.g. Baan, Wood & Haschick 1982). These masers tended to be extremely luminous, and were referred to as megamasers due to them being over a million times more luminous than typical Galactic interstellar OH maser sources (see Lo 2005, for a review).

The OH molecule has four hyperfine transitions due to the coupling of the spin of the unpaired electron with the nuclear spin of the

hydrogen atom. These transitions occur at 1612, 1665, 1667, and 1720 MHz, with line ratios of 1:5:9:1 in local thermodynamic equilibrium. The conditions necessary for maser emission include a source of energy that ensures that there are more molecules in the upper energy level than in the lower, in order to produce the stimulated emission. Indeed, it has become clear over the past few decades that OH megamasers (OHMs) are closely associated with galaxies with significant infrared emission, exhibiting a tight correlation between the far-infrared luminosity and the OHM luminosity (e.g. Baan et al. 2008; Wang et al. 2023). Theoretical models have shown that OHM emission is efficiently produced at relatively high temperatures (~ 80 – 140 K), with a minimum temperature of ~ 45 K needed for inversion (Lockett & Elitzur 2008). However, the dust around star-forming regions in external galaxies tends to be much cooler than this (30–50 K; e.g. Hwang et al. 2010; Smith et al. 2013, 2014). Thus, to produce maser emission in these cooler environments means that the OH gas is likely co-located with the heating source. Willett et al. (2011a, b) investigate the dependence of the OHM luminosity on the mid-infrared emission using data from the Spitzer Infrared Spectrograph to argue that a large smoothly distributed dust reservoir with temperatures from ~ 50 to 100 K and high opacity ($\tau \sim 100$ – 400) is required for OHM emission.

However, there are key differences between using an infrared galaxy survey as a parent sample to look for masers (e.g. Norris et al.

* E-mail: matt.jarvis@physics.ox.ac.uk

1989; Baan, Haschick & Henkel 1992; Staveley-Smith et al. 1992), and a purely spectral line survey that can detect OHMs irrespective of the host galaxy properties (see e.g. Townsend et al. 2001). It is only the latter that allow us to understand the full range of conditions sufficient to produce OHM emission.

To carry out such surveys, one needs large spectral bandwidths at radio wavelengths, where the OH emission is detected ‘blindly’, with no pre-selection of samples such as (ultra)luminous infrared galaxies, (U)LIRGS, and/or mergers (e.g. Darling & Giovanelli 2006). Many of the most successful untargeted surveys for OHMs are nominally focused on detecting and understanding neutral atomic hydrogen via the 21 cm line (e.g. Suess et al. 2016; Haynes et al. 2018; Hess et al. 2021; Roberts, Darling & Baker 2021), due to its relative proximity to the OH maser lines. The vast majority of these surveys have concentrated their efforts on surveying relatively large areas at low redshift in order to cover a large cosmic volume (Darling & Giovanelli 2000, 2001, 2002). However, in order to reach beyond the local Universe, high sensitivity is required, coupled with a relatively large bandwidth that allows a survey to cover a significant amount of cosmic volume by virtue of a deeper sampling in the radial direction, rather than broader areal coverage. One of the key facilities that is able to carry out this type of survey is MeerKAT (Jonas & MeerKAT Team 2016; Camilo et al. 2018), which couples very high sensitivity with a wide bandwidth at both the L - and ultra-high-frequency (UHF) bands. Indeed, Glowacki et al. (2022) have already discovered a high-redshift ($z = 0.52$) OHM using data from the MeerKAT telescope, as part of the Looking At the Distant Universe with the MeerKAT Array (LADUMA) survey (Blyth et al. 2016), and Combes et al. (2021) detected satellite-line absorption against the distant radio source PKS 1830-211 at $z = 0.89$ with known OH main-line absorption (Chengalur, de Bruyn & Narasimha 1999), as part of the MeerKAT Absorption Line Survey (MALS; Gupta et al. 2016).

In this paper, we report the discovery of the most distant OHM found to date from an untargeted survey, using data from the MeerKAT radio telescope as part of the MeerKAT International Gigahertz Tiered Extragalactic Exploration (MIGHTEE; Jarvis et al. 2016) survey. In Section 2, we provide details of the MIGHTEE data and the calibration and imaging procedure used for creating the spectral line cubes. In Section 3, we determine the properties of the OHM and the host galaxy in which it resides and in Section 4 we discuss our results and summarize our conclusions.

Throughout the paper, we assume $H_0 = 67.7 \text{ km s}^{-1} \text{ Mpc}^{-1}$, $\Omega_m = 0.31$, and $\Omega_\Lambda = 0.69$ (Planck Collaboration VI 2020).

2 MIGHTEE OBSERVATIONS

The MIGHTEE survey is one of the Large Survey Projects currently being conducted by the MeerKAT radio telescope in South Africa. It is surveying approximately 20 deg^2 over four of the most widely observed deep extragalactic fields accessible from the Southern hemisphere. It is conducting the bulk of the survey using the L -band receiver, which covers the frequency range 856–1711 MHz. The Early Science data were taken with 4096 channels spanning the L band, which has enabled a broad range of science topics to be addressed using the radio continuum (e.g. Whittam et al. 2022; Hale et al. 2023), spectral line (e.g. Maddox et al. 2021; Ponomareva et al. 2021, 2023), and polarization (e.g. Böckmann et al. 2023) data. Subsequent observations for the MIGHTEE survey were taken at the full resolution offered by MeerKAT after its correlator was upgraded, providing 32 768 channels with a velocity resolution of 5.5 km s^{-1} at 1420 MHz.

The COSMOS field was observed by MeerKAT in 32k channel mode for a total of $15 \times 8 \text{ h}$ tracks in a tightly dithered mosaic that spans around 2 deg^2 at $\sim 1.4 \text{ GHz}$, resulting in 94.2 h of on-field integration. The target-only visibilities for each of these pointings were retrieved from the SARAO archive¹ at full spectral resolution using the KAT Data Access Library,² and with the Level-1 calibrations applied, as derived by the SARAO Science Data Processor. The MIGHTEE spectral line processing divides MeerKAT’s L band into three regions that are relatively free of radio frequency interference (RFI), namely 960–1150, 1290–1520, and 1610–1650 MHz. Each set of visibilities is split into these three sub-bands that are processed independently following Doppler correction to a barycentric reference frame. For the lowest frequency sub-band, the frequency domain is averaged by a factor of 4 to a resolution of 104.5 kHz, as we do not expect to detect low-velocity dispersion emission line sources in the low-frequency band, while the upper two sub-bands retain the full resolution.

Flagging of the visibilities is performed using the TRICOLOUR package (Hugo et al. 2022). Each sub-band is imaged using the WSCLEAN software (Offringa et al. 2014), with a pointing-specific mask for the continuum sources derived from the existing deep MIGHTEE continuum images (Heywood et al. 2022). The spectral clean component model is interpolated using the SMOPS³ tool to provide smoothness in the spectral domain. Following inversion of this model into the visibility domain, a round of (phase + delay) self-calibration and simultaneous subtraction of the smoothed continuum model is performed using the CUBICAL (Kenyon et al. 2018) package.

Each pointing is then imaged on a per-channel basis using WSCLEAN using three robustness (0.0, 0.5, and 1.0) parameters (Briggs 1995), and deconvolution masks are constructed from the resulting image using a custom PYTHON tool (Heywood et al., in preparation). Imaging is repeated with deconvolution within the masked regions, and the resulting per-pointing cubes are homogenized to a common angular resolution per channel, using custom PYTHON code as well as the PYPHER package (Boucaud et al. 2016). These homogenized images are primary beam corrected using the KATBEAM⁴ library, and then linearly mosaicked assuming variance weighting using the MONTAGE⁵ toolkit. A final process of image–plane continuum subtraction is performed using custom PYTHON code along every sightline through the resulting cubes. Full details of the procedure outlined above and the custom methodology involved is provided in Heywood et al. (in preparation). We also note that the MIGHTEE data are taken in full polarization mode, details of which can be found in Taylor et al. (in preparation).

3 THE OH MEGAMASER J095903.22+025356.1

3.1 OH megamaser emission lines

We visually inspected the low-frequency (960–1150 MHz) robust-0.0 spectral-line cube, which has a spatial resolution of $10 \times 15 \text{ arcsec}^2$ and a median rms sensitivity of $\sim 75 \mu\text{Jy}$ per channel (channel width of 104.5 kHz), over the COSMOS field to search for high-redshift emission line galaxies. We discovered a bright, unresolved source at $\text{RA} = 09^{\text{h}}59^{\text{m}}03^{\text{s}}.22 \text{ Dec.} = 02^{\text{d}}53^{\text{m}}56^{\text{s}}.1$

¹<https://archive.sarao.ac.za>

²<https://github.com/ska-sa/katdal>

³<https://github.com/Mulan-94/smops>

⁴<https://github.com/ska-sa/katbeam>

⁵<http://montage.ipac.caltech.edu/>

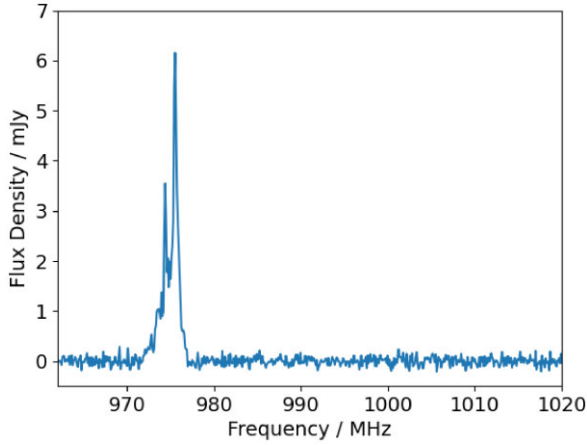


Figure 1. The observed-frame spectrum of the OHM J095903.22+025356.1 from 960 to 1020 MHz. The rms noise across the spectral range spans 70–80 μ Jy per 104.5 kHz channel across this range (see Heywood et al., in preparation for further details).

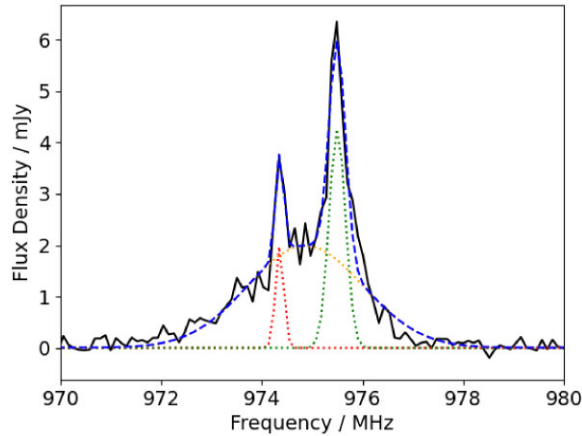


Figure 2. The observed-frame spectrum of the OHM J095903.22+025356.1 (black solid line). The best-fitting ($\chi^2_{\text{red}} = 0.6$) three-Gaussian model (blue dashed line) includes broad emission from a redshifted 1667 MHz line component (orange dotted line), along with narrow 1667 MHz (green dotted line) and 1665 MHz (red dotted line) emission lines.

(J2000), and a frequency of $\nu = 975.31$ MHz with a signal-to-noise ratio (SNR) of ~ 80 at the peak of the line. A second bright emission line centred at $\nu = 974.1$ MHz was also observed at the same position on the sky (SNR = 51 at the peak of the line). The full spectrum, extracted over the restoring clean beam and normalized by the beam area, is shown in Fig. 1 and a zoom in on the 1665 and 1667 MHz region is shown in Fig. 2. These two lines correspond exactly to the rest-frame 1667 and 1665 MHz main emission lines of the OH molecule at $z = 0.7092$. Thus, this is the highest redshift OH main-line megamaser in emission discovered to date,⁶ eclipsing the previous record holder ($z = 0.52$; Glowacki et al. 2022), which was also discovered with MeerKAT.

As can be seen in Fig. 2, the 1667 MHz emission line is bright and relatively narrow, and the 1665 MHz emission line also appears

⁶We note that the highest-redshift OHM in emission remains the tentative satellite-line detection of PKS1830-211 by Combes et al. (2021), which was targeted as part of the MeerKAT Absorption Line Survey.

Table 1. (top) Best-fitting parameters for the three-Gaussian fit to the emission lines, where the broad component is assumed to be the 1665 MHz line at the systemic redshift. (bottom) Best-fitting parameters for the three-Gaussian fit to the emission lines, where the broad component is assumed to be the 1667 MHz line that is redshifted with respect to the systemic velocity of the narrow lines.

OHM properties with broad 1665 line	
z_{spec}	0.7092 ± 0.0001
$\log_{10}(L_{1667}/L_{\odot})$	4.20 ± 0.02
$\log_{10}(L_{1665n}/L_{\odot})$	3.53 ± 0.06
$\log_{10}(L_{1665b}/L_{\odot})$	4.46 ± 0.03
$\text{FWHM}_{1667}/\text{km s}^{-1}$	172 ± 6
$\text{FWHM}_{1665n}/\text{km s}^{-1}$	72 ± 8
$\text{FWHM}_{1665b}/\text{km s}^{-1}$	917 ± 48
χ^2_{red}	1.88
OHM properties with broad redshifted 1667 line	
z_{spec}	0.7092 ± 0.0001
$\log_{10}(L_{1667n}/L_{\odot})$	4.02 ± 0.02
$\log_{10}(L_{1667b}/L_{\odot})$	4.54 ± 0.02
$\log_{10}(L_{1665}/L_{\odot})$	3.4 ± 0.05
$\text{FWHM}_{1667n}/\text{km s}^{-1}$	118 ± 5
$\text{FWHM}_{1667b}/\text{km s}^{-1}$	832 ± 27
$\text{FWHM}_{1665n}/\text{km s}^{-1}$	60 ± 6
Velocity of inflow/ km s^{-1}	333 ± 20
χ^2_{red}	0.60

to have a narrow component. However, there also appears to be a broader underlying component around the 1665 MHz line. We therefore initially fit the emission lines with three Gaussian profiles (two components for the 1665 MHz line and a single component for the 1667 MHz line), with the normalization, width, and redshift left as free parameters (assuming the redshift is the same for all three components). The resulting parameters are listed in Table 1 (top panel).

The ratio of the luminosities of the 1667 and 1665 MHz lines provides information on the physical conditions within the gas clouds from which the OH emission arises (e.g. Darling & Giovanelli 2002). Under the assumption of local thermodynamic equilibrium and optically thin lines, we would expect a line ratio of 1.8, and considering only the narrow 1665 MHz component ($3.4 \times 10^3 L_{\odot}$), we measure a line ratio of 4.7, which is similar to the ratio observed in other OHMs (e.g. McBride, Heiles & Elitzur 2013; Hess et al. 2021). The observed line ratio is compatible with the models in which the main OH lines have non-negligible optical depths (e.g. Lockett & Elitzur 2008).

Unfortunately, we have no constraints on the satellite line at 1612 MHz as it falls below the lower end of the spectral coverage in our L-band data, and we find no evidence for emission at the redshifted 1720 MHz line at 1006.4 MHz. We estimate the limiting flux for the 1720 MHz line of $\sim 150 \mu$ Jy per beam (2σ) for the peak flux, and a corresponding integrated luminosity of $\log_{10}(L/L_{\odot}) = 3.08$ assuming a Gaussian line profile with $\text{FWHM} = 120 \text{ km s}^{-1}$. This leads to a lower limit on the 1667/1720 ratio of >3 , which is again within the range of line ratios exhibited in other lower redshift OHM systems (McBride, Heiles & Elitzur 2013).

Given the very different line widths for the broad component and the 1667 MHz line it is likely that the emission is coming from different regions, one with high velocity dispersion and a region at much lower velocity dispersion. Large gaseous outflows have been observed in infrared luminous galaxies (e.g. Rupke, Veilleux & Sanders 2005; Spoon et al. 2013; Gowardhan et al. 2018). Therefore,

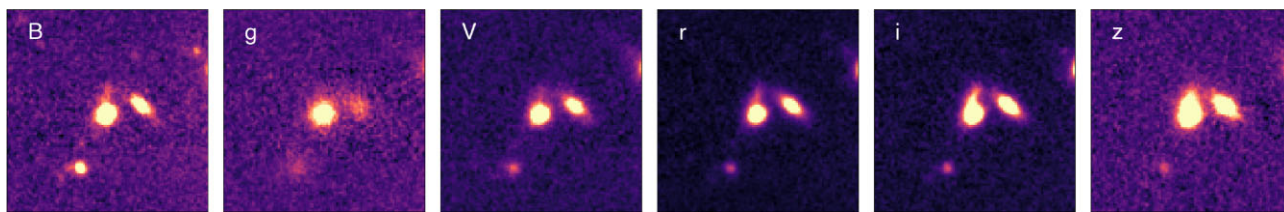


Figure 3. Postage stamps of the OHM host galaxy in B -, g -, V -, r -, i -, and z -band filters from Subaru. The galaxy ~ 2.6 arcsec to the west has a photometric redshift of $z_{\text{phot}} = 0.35$ or 0.43 (see text) and is not associated with the OHM host galaxy. Note that the different filters have different depths and the colour scale is chosen to bring out the key features. The flux density of the OHM host galaxy for each filter is given in Table 2.

a possible second explanation for the broad component is that it is due to a high velocity outflow (or inflow) in the 1667 MHz line. We therefore refit the emission line with an extra free parameter that allows a broad 1667 MHz component to have a different redshift to the systemic redshift. The best-fitting parameters are given in Table 1 (bottom panel) and the fit is shown in Fig. 2. In this case, the inflow/outflow velocity of the 1667 MHz line is $\sim 330 \text{ km s}^{-1}$ and provides a marginally better fit than the assumption of a broad 1665 MHz line (reduced $\chi_{\text{red}}^2 = 0.6$ compared to $\chi_{\text{red}}^2 = 1.88$ for the broad 1665 MHz component model). We note that more complex combinations of broad and narrow line components for the 1665 and 1667 MHz lines could replicate the observed spectrum. However, our current data do not support more complex models as the reduced $\chi_{\text{red}}^2 = 0.6$ for the broad velocity outflow/inflow model, suggests we are already overfitting the observations. To explore this further, higher spatial resolution would be required, which requires longer baselines than currently available to MeerKAT. Thus, we are limited in terms of what we can say about the underlying emission line profiles, other than we find evidence for at least two distinct velocity dispersion components, and that we marginally prefer a model with a broad component that is either inflowing or outflowing with respect to the systemic velocity. We cannot differentiate inflow from outflow from the spectrum alone, due to the fact that we cannot determine whether the high-velocity component is in front of, or behind, the position of the narrow-line components, which we assume to trace the systemic redshift. However, the large width of the broad component is likely due to the large-scale motions of individual maser clouds (e.g. Lockett & Elitzur 2008) and suggests a system which is undergoing some level of disruption, possibly due to a major merger. This second model for the emission-line components reaffirm it as the brightest main-line OHM discovered thus far (see Table 1 for a summary of all the derived properties).

We are able to constrain the pumping efficiency, η_{OH} of the maser emission using the following ratio:

$$\eta_{\text{OH}} = \frac{L_{\text{OH}} \times \Delta\nu_{\text{IR}}}{L_{\text{IR}} \times \Delta\nu_{\text{OH}}}, \quad (1)$$

where L_{OH} is the luminosity of the 1667 MHz OH line and L_{IR} is the infrared luminosity across the $53 \mu\text{m}$ line, which (supplemented by the 35 , 80 , and $120 \mu\text{m}$ lines) can pump the OH molecule (Elitzur 1982; Lockett & Elitzur 2008). $\Delta\nu_{\text{OH}}$ and $\Delta\nu_{\text{IR}}$ are the widths of the OH and IR lines. Using Arp 220 as a local analogue (e.g. He & Chen 2004), we assume pumping line widths $\sim 200 \text{ km s}^{-1}$ and equivalent widths $\sim 0.04 \mu\text{m}$, and determine the rest-frame continuum emission at $53 \mu\text{m}$ from the spectral energy distribution (SED) fit in Fig. 5 (we note that it is very close to the observed frame $100 \mu\text{m}$ measurement from *Herschel* so is well constrained). We find that the $53 \mu\text{m}$ line has an estimated luminosity of $5.2 L_{\odot}$, leading to an OH pumping efficiency of $\gg 100$ per cent for both the narrow and redshifted broad components of the 1667 MHz line. This is not

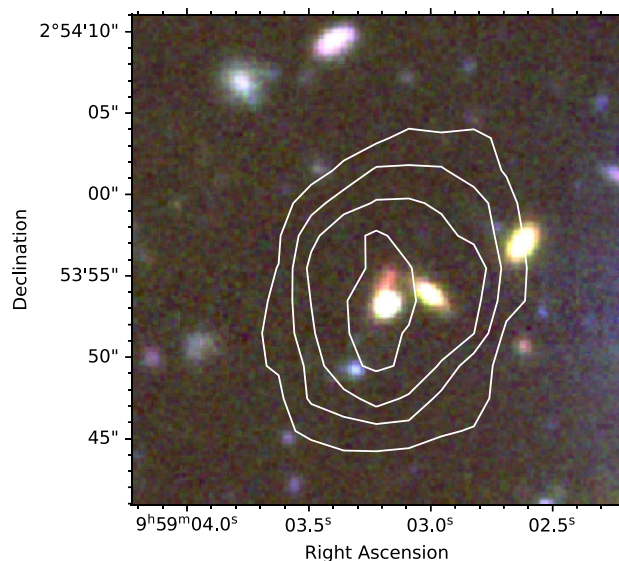


Figure 4. Three-colour (B , V , and i) image of the OHM host galaxy with the OHM emission denoted by the contours (40, 70, 100, and 140 Jy Hz). The OHM is unresolved at the spatial resolution of our data and as such the contours represent the restoring beam.

surprising given the extreme luminosity of the OHM, although as we discuss in Section 3.3, differential lensing may also lead to a much higher OHM luminosity relative to the host galaxy. Given the 45 K dust temperature inferred in Section 3.2, this estimate is in line with the finding of Klöckner (2004), suggesting that those OHM host galaxies with cooler ($< 50 \text{ K}$) infrared emission exhibit greater efficiency ($\gg 1$ per cent), and that the maser emission is saturated. Such saturated maser emission is thought to arise from high-density, optically thick regions ($> 10^5 \text{ cm}^{-3}$) (Elitzur 1982; Darling 2007), which are also some of the strongest maser sources.

3.2 Host galaxy properties

The COSMOS field has been widely observed across the full electromagnetic spectrum, we therefore have a wealth of multiwavelength data with which to measure the properties of the OHM host galaxy. We have identified an optical source at the position of the OHM using the COSMOS2020 catalogue (Weaver et al. 2022). In Fig. 3, we show the B -, g -, V -, r -, i -, and z -band imaging around the OHM from the Subaru telescope, and in Fig. 4 we show the emission from the OHM overlaid on a three-colour optical image. The host galaxy is clear alongside a galaxy 2.6 arcsec away (but at a lower redshift – see Section 3.3). The OHM host galaxy itself appears to have a stream of emission across all visible bands to the north, which may be indicative

Table 2. Measured photometry for the OHM host galaxy from the COSMOS2020 catalogue complemented with mid- and far-infrared data from *WISE*, *Spitzer*, and *Herschel* using products from the *Herschel* Extragalactic Legacy Project (HELP; Shirley et al. 2021) and radio data from MIGHTEE and the VLA 3GHz survey. *WISE* filters with a † superscript are not used in the SED fitting due to better similar wavelength data from *Spitzer*.

Filter	Effective wavelength (μm)	S_{ν} (μJy)	$\sigma_{S_{\nu}}$ (μJy)
<i>u</i>	0.346	1.65	0.02
<i>u</i> *	0.350	2.03	0.03
<i>g</i>	0.460	3.11	0.02
<i>r</i>	0.538	6.68	0.03
<i>i</i>	0.652	12.16	0.03
<i>z</i>	0.866	15.36	0.05
<i>y</i>	0.906	19.68	0.08
IRAC1	3.56	71.1	0.2
IRAC2	4.51	82.8	0.2
IRAC3	5.76	304	7
IRAC4	8.00	2076	80
W1†	3.37	72.0	14.4
W2†	4.62	99.2	19.8
W3	12.08	3003	600
W4	22.19	2813	560
MIPS	24	2785	347
PACS100	100	164 496	435
PACS160	160	151 030	540
SPIRE250	250	78 641	834
SPIRE350	350	36 268	1396
SPIRE500	500	8146	2807
Radio band	Effective frequency	S_{ν} (μJy)	$\sigma_{S_{\nu}}$ (μJy)
<i>L</i> band	1.19 GHz	250	9
<i>S</i> band	3.0 GHz	118	7

of an interaction, i.e. a tidal tail from a merger event. However, the ground-based data are not high enough resolution to disentangle this emission and confirm whether it is due to a merger. Unfortunately, the OHM falls outside the *HST* coverage of the COSMOS field. The other possibility is that this elongated emission is due to gravitational lensing by the nearby galaxy in projection and lies at a lower redshift, and we return to this possibility in Section 3.3.

The available *u* band through to *Spitzer*/IRAC photometry is presented in Table 2, supplemented with mid-infrared data from the *Wide-field Infrared Survey Explorer* (*WISE*) and the *Spitzer Space Telescope* and far-infrared data from the *Herschel Space Observatory* using the *Herschel* Extragalactic Legacy Project (HELP) data base⁷ (Shirley et al. 2021). We are also able to measure the radio continuum flux from both the MIGHTEE data itself, with an effective frequency of 1.2GHz at the position of the OHM (Heywood et al. 2022), and using the VLA 3GHz survey of the COSMOS field (Smolčić et al. 2017).⁸

In order to determine the properties of the host galaxy, we use MAGPHYS (da Cunha, Charlot & Elbaz 2008) to perform a fit to the SED, in which the energy absorbed in the UV part of the spectrum is balanced with the energy re-emitted at far-infrared wavelengths. The best-fitting SED along with the measured photometry is shown in Fig. 5 and the best-fitting parameters are presented in Table 3

⁷<https://hedam.lam.fr/HELP/>

⁸We note that the VLA 3GHz data may resolve out some emission from this host galaxy, see e.g. Hale et al. (2023).

after fixing the redshift to $z = 0.7092$, assuming a Chabrier initial mass function (Chabrier 2003). We are able to obtain a very good fit to the vast majority of the photometric data (the exception being the measurement at $8 \mu\text{m}$, which we return to below). The key derived properties suggest a rapidly star-forming galaxy with a star formation rate (SFR) of $371 \pm 20 M_{\odot} \text{yr}^{-1}$ and a total stellar mass of $\log_{10}(M_{\star}/M_{\odot}) = 10.5 \pm 0.2$, which together means that it lies approximately 1.5 dex above the star-forming galaxy main sequence at this redshift (e.g. Whitaker et al. 2014; Johnston et al. 2015). The stellar mass derived from MAGPHYS is also consistent with that determined in the COSMOS2020 catalogue, which reports a total stellar mass of $\log_{10}(M_{\star}/M_{\odot}) = 10.31 \pm 0.04$. However, we find a much higher SFR compared to the value in the COSMOS2020 catalogue ($\approx 50 M_{\odot} \text{yr}^{-1}$), which is unsurprising given the level of dust extinction from the model fit ($A_V = 2.94$) and the significant amount of obscured star formation evidenced from the high far-infrared luminosity of $L_{\text{IR}} = 3.6 \times 10^{12} L_{\odot}$, which confirms the host galaxy as an ULIRG.

Such galaxy properties are similar to the host galaxies of OHMs in the local Universe, where there is a strong correlation between the OHM luminosity and the far-infrared luminosity (e.g. Darling & Giovannelli 2002, 2006; Zhang et al. 2014). To highlight the properties of this OHM, in Fig. 6 we show the OH luminosity against far-infrared luminosity for a complete sample of OHM galaxies at $z < 0.5$ from the compilation Roberts & Darling (in preparation) and the OHM at $z = 0.52$ from Glowacki et al. (2022). The $z = 0.7092$ OHM discussed in this paper is clearly the brightest OHM thus far discovered, but the far-infrared luminosity is also very high, such that it lies along the known correlation. Thus, although very luminous, its ratio between far-infrared and OH luminosities is not significantly different from the low-redshift populations.

As mentioned earlier, one interesting detail in the SED is that the measured flux in IRAC Channel 4 at $8 \mu\text{m}$ is around 1.5 dex higher than the best-fitting SED. This is the only measurement that does not agree within the uncertainties with the best-fitting SED, and is such an extreme outlier it warrants discussion. We note that the galaxy is also very bright in the *W3* filter, with a very red colour between the *W2* and *W3* bands, thus confirming that the $8 \mu\text{m}$ emission is unlikely to be a spurious measurement. One possible explanation is that the total SED could be a combination of multiple galaxies within the point spread function (PSF) of the $8 \mu\text{m}$ data. However, the only galaxy that is nearby is ~ 2.6 arcsec away and does not appear to show a strong increase in flux from the 3.6 to $8 \mu\text{m}$ bands in the COSMOS2020 catalogue, where $S_{3.6} = 9.86 \mu\text{Jy}$ and $S_8 = 22.5 \mu\text{Jy}$ (compared to the flux from the maser host galaxy of $S_8 = 2076 \mu\text{Jy}$). We therefore rule out contamination from the projected nearby galaxy. Moreover, as can be seen in Fig. 5, the other mid-infrared bands all require significant emission from polycyclic aromatic hydrocarbons (PAHs); in particular the rest-frame $3.3 \mu\text{m}$ feature is needed to fit the $5.8 \mu\text{m}$ photometry. The presence of strong PAHs is not unusual in OHM host galaxies (e.g. Willett et al. 2011a), again suggesting that the OHM presented here is not anomalous and has very similar properties to the vast majority of other OHM host galaxies.

Another possible explanation for the excess emission in the $8 \mu\text{m}$ band could be hot dust emission from a torus around an accreting active galactic nucleus (AGN). We therefore use the CIGALE SED fitting code (Boquien et al. 2019) to attempt to fit a composite AGN + galaxy SED. We adopt parameters similar to those used in studies of radio-selected AGNs (Best et al. 2023; Zhu et al. 2023) and more broadly selected galaxy samples (Zou et al. 2022), which incorporate two models for AGN emission from both the accretion disc and the obscuring torus (Fritz, Franceschini & Hatziminaoglou

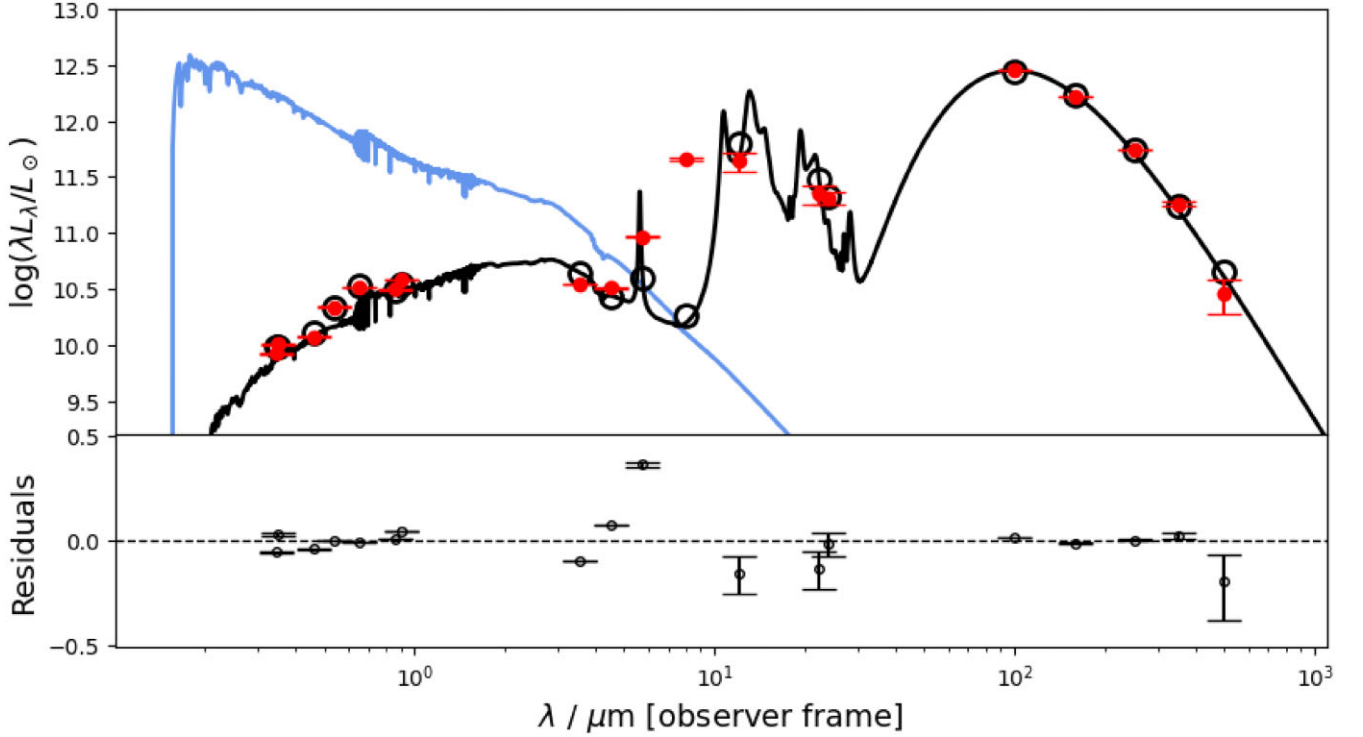


Figure 5. SED of the OHM host galaxy with the best fit to the combined optical, near-infrared, and far-infrared SED, derived using MAGPHYS (black line). The blue line represents the intrinsic stellar spectrum that has been reddened with $A_V = 2.94$ in order to fit both the optical and near-infrared data and the reprocessed dust emission at mid- to far-infrared wavelengths. The red solid circles are the observed photometry, and the open black circles denote the predicted photometry from the best-fitting model. The best-fitting parameters are listed in Table 3. The residuals of the fit with respect to the data are presented in the lower panel. The point at $8 \mu\text{m}$ lies ~ 1.6 dex above the best-fitting SED and is therefore not shown in the lower panel.

Table 3. Best-fitting parameters for the SED from MAGPHYS. SFR in the radio is calculated assuming the measured spectral index between 1.2 and 3 GHz, and the flux at 3 GHz from VLA COSMOS.

Host galaxy properties	
z_{phot}	$0.706^{+0.09}_{-0.08}$
$\log_{10}(M_*/M_{\odot})$	10.47 ± 0.2
$\text{SFR}_{\text{SED}} (M_{\odot} \text{ yr}^{-1})$	371 ± 20
$\text{SFR}_{\text{Radio}} (M_{\odot} \text{ yr}^{-1})$	342 ± 68
$\log_{10}(\text{sSFR}_{\text{SED}} / \text{yr}^{-1})$	-7.92 ± 0.6
$\log_{10}(L_{\text{dust}}/L_{\odot})$	12.56 ± 0.02
$T_{\text{dust}} / \text{K}$	45 ± 2
$\log_{10}(M_{\text{dust}}/M_{\odot})$	8.27 ± 0.04
A_V	2.94 ± 0.02
$\log_{10}(L_{1.4\text{GHz}} / \text{W Hz}^{-1})$	23.90 ± 0.04

2006; Stalevski et al. 2012, 2016), alongside stellar population synthesis models from Bruzual & Charlot (2003). However, there is no combination that can reproduce the high luminosity within the $8 \mu\text{m}$ band, while also still adequately fitting the range of other multiwavelength data. We are likewise not aware of any spectral feature that could be boosting the $8 \mu\text{m}$ flux density at the redshift of the OHM system.

In order to check whether there are any other signatures from an AGN component, we make use of the radio continuum imaging data from both the MIGHTEE data and the VLA COSMOS 3 GHz survey (Smolčić et al. 2017). We measure a flux density at 1.2 GHz of $S_{1.2\text{GHz}} = 250 \pm 9 \mu\text{Jy}$, which corresponds to a $\text{SFR} = 342 \pm 68 M_{\odot} \text{ yr}^{-1}$; the uncertainty encompasses the systematic uncertainty of

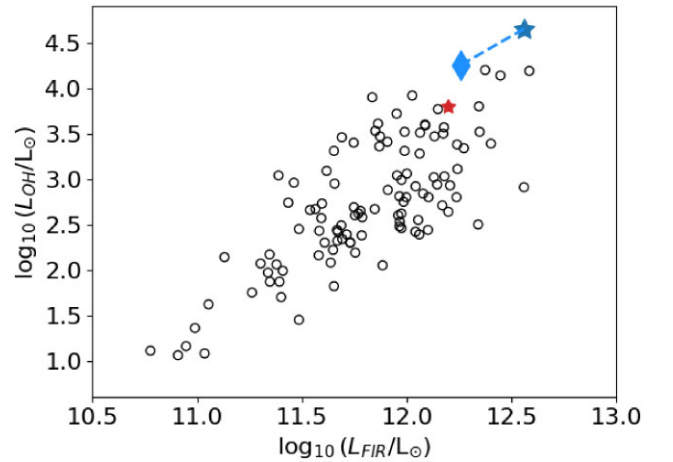


Figure 6. The far-infrared–OHM luminosity relation for the sample of OHMs from Roberts & Darling (in preparation) (open circles), the OHM from Glowacki et al. (2022) (red star), and the OHM: J95903.22+025356.1, presented in this paper (blue star). The OHM luminosity shown is the combination of the broad- and narrow-1667 MHz emission line luminosities. The dashed line towards the light-blue diamond denotes where the OHM and host galaxy would lie if the OHM was magnified by a factor of 2.5 and the host by a factor of 2 (the two most likely lensing magnifications).

using different conversions from 1.4 GHz to a SFR from Bell (2003), Delhaize et al. (2017), and Delvecchio et al. (2021). Thus, the SFR using the best-fitting MAGPHYS SED is completely consistent with the SFR estimated from the radio continuum. Moreover, the

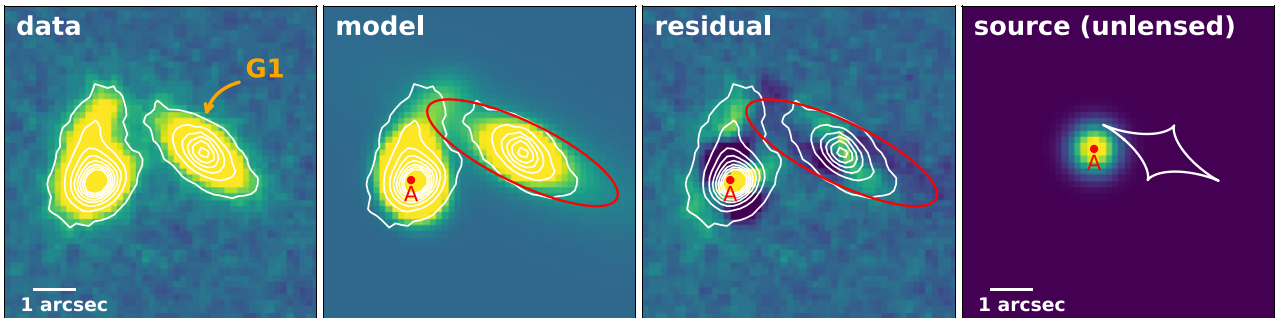


Figure 7. Left: Data from the Subaru *i*-band image and overlaid white self-contours, with galaxy G1 labelled. Middle left: Median posterior model from the single lens model convolved with the PSF. The critical curve is overlaid in red and the median image–plane position of the source centroid is labelled ‘A’. A point source at this location has a magnification of $\mu_{\text{pt,A}} = 20.4$, while the entire source has a magnification $\mu_{\text{tot}} = 1.8$. Middle right: residual image (data – model) with data contours, critical curve, and point A indicated. Right: Source plane representation of the lensing with a circular Gaussian of radius $R_{\text{src}} = 0.25$ arcsec. The caustic curve is shown in white and the image stretch ranges from the zero to the peak of the source-plane Gaussian. As can be seen, the centroid ‘A’ lies very near the cusp caustic. The scale-bar corresponds to the source plane.

radio continuum emission is unresolved at the highest resolution of both the MIGHTEE data (~ 5 arcsec) and the VLA COSMOS data (~ 0.7 arcsec). Taken together, the radio emission does not provide any indication that there may be a contribution to the SED from an AGN.⁹ Therefore, although the SED fit and the radio continuum measurements are consistent, the excess emission at mid-infrared wavelengths remains a puzzle and will require much higher resolution mid-infrared data to resolve, e.g. from *JWST*.

We can also use the measurements from *WISE* and *Spitzer*/IRAC to determine where the host galaxy of the megamaser resides in colour space compared to the broader classifications of galaxy populations. Using the colour–colour plots from Roberts, Darling & Baker (2021), who investigate where the host galaxies of masers should reside compared to those of H I galaxies, we find that the host galaxy of OHM J095903.22+025356.1 has *WISE* and IRAC colours fully consistent with the local OHM host galaxy population. However, we note it has a relatively red $W2 - W3 = 6.15$ mag, meaning it lies at the extreme red end of the ULIRG population in the *WISE* colour–colour diagram of Jarrett et al. (2011). The extreme $W2 - W3$ colour is partly due to the fact that the *W2* and *W3* bands are sampling the rest-frame ~ 2.7 and ~ 7.1 μm emission, and that at these rest wavelengths, the PAH emission contributes significantly to the measured photometry, particularly in the *W3* filter. However, we note the $W1 - W2 = 0.714$ colour is very much in the middle of the expected range for ULIRGs and starburst galaxies and lies within the colour range expected for OHM host galaxies (see e.g. Roberts, Darling & Baker 2021; Glowacki et al. 2022), with this emission predominantly arising from old stellar populations, rather than warm dust and PAH emission.

3.3 Lensing

Given the very high luminosity of the OH emission line and the stream of emission to the north of the OHM host galaxy (Fig. 3), it is worth assessing whether the system could be gravitationally lensed. The host galaxy mass and SFR are not extreme, however, suggesting that the host is unlikely to be significantly lensed. If the OHM originates from a very compact region within the host galaxy,

then differential lensing could still provide significant magnification to the emission lines. There is a galaxy 2.6 arcsec away from the OHM host galaxy (the galaxy lying directly to the west in Figs 3, 4, and 7, referred to as G1), which is present in the COSMOS2020 catalogue. It has a best-fitting photometric redshift of $z_{\text{phot}} = 0.43^{+0.02}_{-0.03}$ and stellar mass of $\log_{10}(M_{\star}/M_{\odot}) = 9.56$ using LE PHARE (Ilbert et al. 2006) and $z_{\text{phot}} = 0.35 \pm 0.01$ and $\log_{10}(M_{\star}/M_{\odot}) = 9.75$ derived using EAZY (Brammer, van Dokkum & Coppi 2008).

The Einstein radius for a lens of this mass and redshift (similar for both photometric redshifts) is ~ 1.1 arcsec, assuming a halo mass of $M_{\text{halo}} = 3.2 \times 10^{11} M_{\odot}$, estimated using an empirically derived stellar-mass to halo-mass ratio (Behroozi, Conroy & Wechsler 2010).

The primary aim of our lens modelling is to estimate a plausible magnification factor range of the OH emission, which is spatially unresolved with the MeerKAT 10×15 arcsec beam. Our objective is to robustly constrain a macro lens model, rather than precise non-parametric reconstruction of the stellar light distribution. This approach is taken for the following reasons: (i) the ~ 0.7 arcsec seeing of the ground-based data limits the inference possible for this high ellipticity, small Einstein ring foreground lens; (ii) the lack of constraints from unambiguously identified multiply lensed images; and (iii) the expectation that the source has an intrinsically complex, asymmetric morphology that is typical of ULIRGS (e.g. Clements et al. 1996; Veilleux, Kim & Sanders 2002; Yuan, Kewley & Sanders 2010; Larson et al. 2016).

We perform our lens modelling analysis with the LENSTRONOMY¹⁰ package (Birrer & Amara 2018; Birrer et al. 2021), enabling a Bayesian approach to the lens model parameter estimation. We employ the Particle Swarm Optimization non-linear fitting routine to provide the starting point for the Markov chain Monte Carlo sampler, as described in Birrer, Amara & Refregier (2015).

We explore two lens models: the first is the ‘single lens model’ with the closest galaxy (G1) as the only lens, with a projected separation of 2.4 arcsec, the second model, the ‘two lens model’, includes a more distant galaxy (G2) which is 9.1 arcsec away to the north-west (and can be seen in Fig. 4), and may perturb both the convergence and shear of the lensing system. G2 is also listed in the COSMOS2020 catalogues and has a photometric redshift of $z_{\text{phot}} = 0.35$, with stellar

⁹We note that the position of the OHM is not covered by Chandra X-ray survey over the COSMOS field (Civano et al. 2016).

¹⁰<https://github.com/lenstronomy/lenstronomy>

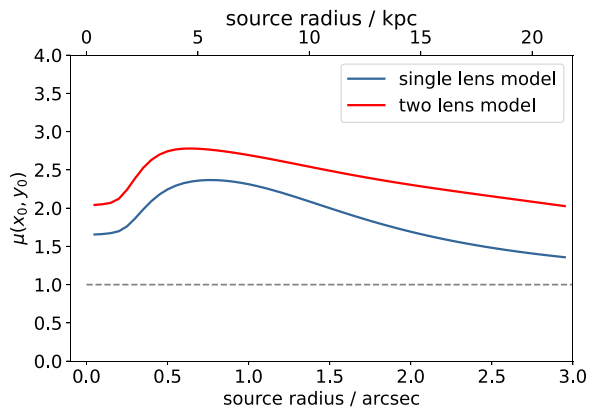


Figure 8. Magnification, μ , as a function of source-plane radius for a circular Gaussian located at the median value of the centroid posterior probability density functions, (x_0, y_0) . The blue and red curves correspond to the single lens model and two lens model, respectively, with the latter showing systematically higher magnification. The ‘bump’ seen at 0.5–1 arcsec is a result of the source size enveloping the entire caustic, resulting in higher total magnification.

mass $M_* = 1.9 \times 10^{10} M_\odot$ ($M_{\text{halo}} = 8.8 \times 10^{11} M_\odot$), which has an Einstein radius of $\theta_E = 1.8$ arcsec.

Both models assume Single Isothermal Ellipsoid (SIE) mass density profiles for the foreground lens(es) and lens redshift(s) of $z = 0.35$. Both models also assume lens light follows mass (i.e. the lens light and mass distributions have co-located centroids and matching ellipticity and position angle). We first fit the G1 galaxy light profile without considering any lensing (i.e. $\theta_E = 0$), deriving a Sérsic index of $n_s = 3.74$. We find that MCMC convergence for all subsequent lens modelling (i.e. $\theta_E > 0$) requires that we fix the main lens light profile Sérsic index to this value. We note that if there is a counter-image blended with the lens light, this approach may bias the lens light profile, and, hence the derived lens model. We test the sensitivity to this assumption by fixing the Sérsic index at a few values in the range $3 < n_s < 4$ and find consistent lens models within the statistical uncertainties. For the two lens model, the Sérsic index of G2 is a free parameter, with a median posterior value of $n_s = 2.31 \pm 0.02$. Both lens models assume a circular Gaussian source, as we find large degeneracies in any model that deviates from this simplistic assumption. The resultant residuals are large, as one would expect, but given our objective of macro lens model constraints with the available data, we find this an appropriate level of model complexity.

Using the single lens model we find a lens Einstein radius for G1 of $\theta_E = 1.32 \pm 0.16$ arcsec, while with the two lens model we find a slightly lower value of $\theta = 1.16 \pm 0.16$ arcsec. The uncertainty is dominated by the systematics of lens model selection, and we assign an indicative uncertainty as the difference between the two derived values. Both of the Einstein radius values are comparable to that derived from the estimated halo mass, $\theta_{E, \text{halo}} = 1.08$ arcsec. This supports both the lensing hypothesis and the derived macro lens models. In Fig. 7, we show the results of the single lens model.

In Fig. 8, we show the lensing magnification expected for a source at the redshift of the OHM as a function of angular and physical source size for both lens models. This shows that if the OHM is relatively compact ($\lesssim 1$ arcsec), then the magnification could be of the order of $\mu \sim 2.5\text{--}3.5 \pm 1.0$, where the uncertainty is assumed to be dominated by the systematic uncertainty between the two models, which has an average of 36 per cent for radii between 0.05 and 3

arcsec. Even larger magnifications ($\mu > 5$) are possible if the OHM is very compact (≤ 0.1 arcsec) and the OHM happens to lie closer to the caustic than the centroid of the optical emission, as could easily happen in a complex merging system. The physical size of OHM emitting regions observed with Very Long Baseline Interferometry (VLBI) show them to be compact (1–100 pc in size; Chapman et al. 1990; Lonsdale et al. 1994; Diamond et al. 1999; Polatidis & Aalto 2000; Klöckner, Baan & Garrett 2003; Rovilos et al. 2003; Pihlström et al. 2005; Momjian et al. 2006; Baan et al. 2023), thus a higher degree of lensing is plausible.

However, even with this lensing magnification (and assuming no lensing of the more extended host galaxy) it would still remain consistent with the $L_{\text{FIR}}\text{--}L_{\text{OHM}}$ relation (see lower point in Fig. 6). This differential lensing of compact components near the host galaxy nucleus in a near cusp-caustic lensing configuration is very similar to that seen in Deane et al. (2013a, b), where the compact AGN core had an order of magnitude higher magnification factor than the stellar and cold molecular gas emission. We note that the lens model cannot account for all of the emission to the north of the OHM host galaxy (see residual in Fig. 7). The most likely reason for this emission is due to an interaction, combined with the limitations of a simple circular Gaussian source model.

Given the likelihood of lensing of a compact OHM towards the centre of the host galaxy, it is worth revisiting the excess emission around $8 \mu\text{m}$. A very compact region of hot dust could be both very bright around the $8 \mu\text{m}$ region and, given the lensing probability, magnified in the same way as the OHM (or more, depending on how compact the region is and where it reside with respect to the caustic). If we assume that the hottest dust is emitted from the inner parts of a putative torus around a supermassive black hole, which is the most likely source of such compact hot dust, then the typical radius is 1–10 pc (Tristram et al. 2009; Tristram & Schartmann 2011), similar in size to OHM emission regions. Thus, differential lensing of a very compact hot dusty region could magnify the mid-infrared emission by a similar amount to the OHM emission, and possibly more depending on the geometry and distribution of the dust. Again, it is very difficult to determine the actual amount of magnification with the resolution of the ground-based data, and this becomes even more difficult at the longer wavelengths, where we are currently reliant on *WISE* and *Spitzer* data which have much poorer resolution than the visible-wavelength data. However, we note that such an additional source of emission at mid-infrared wavelengths would also likely remove the requirement to have such strong PAH emission as currently required in the SED fit shown in Fig. 5 and reduce the large residuals (shown in the lower panel of Fig. 5) at these mid-infrared wavelengths. This is because a significant fraction of the mid-infrared emission could originate from the hot dusty torus, and would therefore be magnified. The degree of magnification would depend on both the temperature distribution and the spatial distribution of the dust. It is clear that there are many uncertainties around this system, both due to the possible lensing and the likelihood of an ongoing merger, and the current data preclude us from investigating this further. Thus, higher resolution multiwavelength observations with *JWST* are needed to resolve the question of lensing in this object, and to understand the system more fully.

4 CONCLUSIONS

We have presented details of the most distant known OHM in the main OH lines discovered thus far at a redshift of $z = 0.7092$. Analysis of the spectrum of the OHM suggests that there are two velocity components that produce the overall line profile, one in which the

OHM gas has a relatively low velocity dispersion (FWHM ~ 100 km s $^{-1}$) and from which we observe both the 1665 and 1667 MHz lines from the OHM molecule. The second component is significantly broader, with a full width at half-maximum of 832 km s $^{-1}$ and is redshifted with a velocity of 333 km s $^{-1}$ relative to the narrow OHM lines. This latter component could be either an inflow or outflow (depending on whether it lies in front of or behind the region responsible for the narrow emission). However, the optical imaging shows what appears to be a tidal-tail feature similar to what is expected from a gas-rich merger, that cannot be explained by gravitational lensing. We therefore infer that the broad velocity component is dynamically separate from the galaxy from which the narrower OHM emission lines arise. The merger process also naturally produces sufficiently high infrared luminosity to pump the OH molecules and produce the very high luminosity of the OHM line ($L_{1667} > 10^4 L_{\odot}$).

We fit the host galaxy SED and find that the host is consistent with the properties of OHM galaxies in the local Universe, i.e. having a high SFR (SFR $\sim 350 M_{\odot} \text{ yr}^{-1}$) and high dust obscuration. The measured SFR and stellar mass of the host suggest that it lies 1.5 dex above the star-forming galaxy main sequence at this redshift. The close agreement between SFR estimated from the SED fitting and the radio continuum measured at both 1.2 and 3 GHz suggests that there is no evidence for AGN-related emission from the host. Indeed, we do not find a combined galaxy + AGN SED model that could reproduce the measured photometry. However, the OHM host galaxy lies in close proximity to a galaxy 2.6 arcsec away in projection (at $z \sim 0.35$) which may be gravitationally lensing the OHM emission (and possibly compact hot dust emission from an AGN torus for example, around observed wavelengths of $\sim 8 \mu\text{m}$). The lensing magnification depends on the exact size and location of the OHM emission region, with magnification factors $\mu \sim 2.5$ for emission regions on the ~ 1 arcsec scale of the host galaxy, but potentially higher ($\mu > 5$) if the emitting regions are similar in size to OHM emission regions in local galaxies and displaced towards the lensing caustic. However, the ground-based data preclude us from making stronger statements on the level of magnification of the OHM and the hot dust emission. We note that the gravitational lensing would produce similar magnification factors to both the optical and infrared data that trace the star formation and the near-infrared data that traces the stellar mass, if they arise on similar spatial scales. Thus the interpretation of a starburst galaxy still holds in the event of significant gravitational lensing.

The discovery of this OHM, along with another high-redshift megamaser recently discovered by MeerKAT (Glowacki et al. 2022), points towards a plausible new window on the obscured galaxy population at high redshift, providing an observational realization of previous proposals (Briggs 1998; Townsend et al. 2001; Darling & Giovanelli 2002). The fact that two new megamasers have been found at $z > 0.5$ within just two of the MeerKAT fields thus far analysed suggests that many more will be discovered with the full MIGHTEE survey, which has a factor of ~ 10 more area than analysed to date, albeit at slightly lower sensitivity. Indeed, assuming approximately one OHM per MeerKAT primary beam at ~ 1 GHz, using the OHM discussed in this paper and that found by Glowacki et al. (2022) as a guide, then we should expect to find around 10–20 more high-redshift ($0.45 \lesssim z \lesssim 0.8$) OHMs over the full MIGHTEE survey area (Jewell et al., in preparation). This effort should lead to new constraints on the evolution of the most obscured systems in the Universe and possibly an independent measure of the gas-rich galaxy merger rate (e.g. Briggs 1998). These new discoveries will come from spectral line surveys, meaning that the uncertainty in photometric

redshifts, particularly for these very obscured systems, is negated (although some uncertainty may remain around confusion between OH and HI lines; Suess et al. 2016; Roberts, Darling & Baker 2021). Therefore, as we move to ever deeper and wider spectral line surveys spanning a large spectral bandwidth, three-dimensional spectroscopic information for some of the most dusty systems in the Universe will become available.

ACKNOWLEDGEMENTS

We would like to thank the anonymous referee for useful comments that improved the manuscript. The MeerKAT telescope is operated by the South African Radio Astronomy Observatory, which is a facility of the National Research Foundation, an agency of the Department of Science and Innovation. We acknowledge the use of the ilifu cloud computing facility – www.ilifu.ac.za, a partnership between the University of Cape Town, the University of the Western Cape, Stellenbosch University, Sol Plaatje University, and the Cape Peninsula University of Technology. The ilifu facility is supported by contributions from the Inter-University Institute for Data Intensive Astronomy (IDIA – a partnership between the University of Cape Town, the University of Pretoria and the University of the Western Cape), the Computational Biology division at UCT, and the Data Intensive Research Initiative of South Africa (DIRISA). MJJ acknowledges generous support from the Hintze Family Charitable Foundation through the Oxford Hintze Centre for Astrophysical Surveys. MJJ, IH, and AAP acknowledge support of the Science and Technology Facilities Council (STFC) consolidated grants [ST/S000488/1] and [ST/W000903/1] and MJJ, IH, SMJ, and HP from a United Kingdom Research and Innovation (UKRI) Frontiers Research Grant [EP/X026639/1], which was selected by the European Research Council. IH acknowledges support from the South African Radio Astronomy Observatory which is a facility of the National Research Foundation (NRF), an agency of the Department of Science and Innovation (DSI). RPD acknowledges funding by the South African Research Chairs Initiative of the DSI/NRF (Grant ID 77948). AJB acknowledges support from the National Science Foundation through grant AST-2308161 and from the Radcliffe Institute for Advanced Study at Harvard University. AB, FS, and GR acknowledge support from the Istituto Nazionale Di Astrofisica (INAF) under the Large Grant 2022 funding scheme (project ‘MeerKAT and LOFAR Team up: a Unique Radio Window on Galaxy/AGN co-Evolution’). MV acknowledges financial support from the Inter-University Institute for Data Intensive Astronomy (IDIA), a partnership of the University of Cape Town, the University of Pretoria, and the University of the Western Cape, and from the South African Department of Science and Innovation’s National Research Foundation under the ISARP RADIOSKY2020 and RADIOMAP + Joint Research Schemes (DSI-NRF grant numbers 113121 and 150551) and the SRUG HIPPO Projects (DSI-NRF grant numbers 121291 and SRUG22031677). This research made use of ASTROPY,¹¹ a community-developed core PYTHON package for Astronomy (Astropy Collaboration 2013, 2018). This research has made use of the Cube Analysis and Rendering Tool for Astronomy (CARTA; Comrie et al. 2021). This research has made use of NASA’s Astrophysics Data System. This research made use of Montage, which is funded by the National Science Foundation under grant number ACI-1440620, and was previously funded by the National

¹¹<http://www.astropy.org>

Aeronautics and Space Administration’s Earth Science Technology Office, Computation Technologies Project, under Cooperative Agreement Number NCC5-626 between NASA and the California Institute of Technology.

DATA AVAILABILITY

The MeerKAT visibility data for the MIGHTEE project are available from the SARAO archive under proposal IDs SCI-20180516-KH-01 and SCI-20180516-KH-02. A public release of the reduced image and catalogue products for the first MIGHTEE spectral line data release covering the COSMOS field is imminent (Heywood et al., in preparation).

REFERENCES

Astropy Collaboration, 2013, *A&A*, 558, A33
 Astropy Collaboration, 2018, *AJ*, 156, 123
 Baan W. A., Wood P. A. D., Haschick A. D., 1982, *ApJ*, 260, L49
 Baan W. A., Haschick A., Henkel C., 1992, *AJ*, 103, 728
 Baan W. A., Henkel C., Loenen A. F., Baudry A., Wiklind T., 2008, *A&A*, 477, 747
 Baan W. A., Aditya J. N. H. S., An T., Klöckner H.-R., 2023, *MNRAS*, 523, 5487
 Behroozi P. S., Conroy C., Wechsler R. H., 2010, *ApJ*, 717, 379
 Bell E. F., 2003, *ApJ*, 586, 794
 Best P. N. et al., 2023, *MNRAS*, 523, 1729
 Birrer S., Amara A., 2018, *Phys. Dark Univ.*, 22, 189
 Birrer S., Amara A., Refregier A., 2015, *ApJ*, 813, 102
 Birrer S. et al., 2021, *J. Open Source Softw.*, 6, 3283
 Blyth S. et al., 2016, Proc. Sci., LADUMA: Looking at the Distant Universe with the MeerKAT Array. SISSA, Trieste, PoS#4
 Böckmann K. et al., 2023, *A&A*, 678, A56
 Boquien M., Burgarella D., Roehlly Y., Buat V., Ciesla L., Corre D., Inoue A. K., Salas H., 2019, *A&A*, 622, A103
 Boucaud A., Bocchio M., Abergel A., Orioux F., Dole H., Hadj-Youcef M. A., 2016, *A&A*, 596, A63
 Brammer G. B., van Dokkum P. G., Coppi P., 2008, *ApJ*, 686, 1503
 Briggs D. S., 1995, American Astronomical Society Meeting Abstracts, #112.02
 Briggs F. H., 1998, *A&A*, 336, 815
 Bruzual G., Charlot S., 2003, *MNRAS*, 344, 1000
 Camilo F. et al., 2018, *ApJ*, 856, 180
 Chabrier G., 2003, *PASP*, 115, 763
 Chapman J. M., Staveley-Smith L., Axon D. J., Unger S. W., Cohen R. J., Pedlar A., Davies R. D., 1990, *MNRAS*, 244, 281
 Chengalur J. N., de Bruyn A. G., Narasimha D., 1999, *A&A*, 343, L79
 Civano F. et al., 2016, *ApJ*, 819, 62
 Clements D. L., Sutherland W. J., McMahon R. G., Saunders W., 1996, *MNRAS*, 279, 477
 Combes F. et al., 2021, *A&A*, 648, A116
 Comrie A. et al., 2021, *CARTA: The Cube Analysis and Rendering Tool for Astronomy*, Zenodo
 da Cunha E., Charlot S., Elbaz D., 2008, *MNRAS*, 388, 1595
 Darling J., 2007, *ApJ*, 669, L9
 Darling J., Giovanelli R., 2000, *AJ*, 119, 3003
 Darling J., Giovanelli R., 2001, *AJ*, 121, 1278
 Darling J., Giovanelli R., 2002, *AJ*, 124, 100
 Darling J., Giovanelli R., 2006, *AJ*, 132, 2596
 Deane R. P., Heywood I., Rawlings S., Marshall P. J., 2013a, *MNRAS*, 434, 23
 Deane R. P., Rawlings S., Garrett M. A., Heywood I., Jarvis M. J., Klöckner H. R., Marshall P. J., McKean J. P., 2013b, *MNRAS*, 434, 3322
 Delhaize J. et al., 2017, *A&A*, 602, A4
 Delvecchio I. et al., 2021, *A&A*, 647, A123

Diamond P. J., Lonsdale C. J., Lonsdale C. J., Smith H. E., 1999, *ApJ*, 511, 178
 Elitzur M., 1982, *Rev. Mod. Phys.*, 54, 1225
 Fritz J., Franceschini A., Hatziminaoglou E., 2006, *MNRAS*, 366, 767
 Glowacki M. et al., 2022, *ApJ*, 931, L7
 Gowardhan A. et al., 2018, *ApJ*, 859, 35
 Gupta N. et al., 2016, Proc. Sci., The MeerKAT Absorption Line Survey (MALS). SISSA, Trieste, PoS#14
 Hale C. L. et al., 2023, *MNRAS*, 520, 2668
 Haynes M. P. et al., 2018, *ApJ*, 861, 49
 He J. H., Chen P. S., 2004, *New Astron.*, 9, 545
 Heiles C. E., 1968, *ApJ*, 151, 919
 Hess K. M. et al., 2021, *A&A*, 647, A193
 Heywood I. et al., 2022, *MNRAS*, 509, 2150
 Hugo B. V., Perkins S., Merry B., Mauch T., Smirnov O. M., 2022, in Ruiz J. E., Pierfederci F., Teuben Peds, ASP Conf. Ser. Vol. 532, Astronomical Data Analysis Software and Systems XXX. Astron. Soc. Pac., San Francisco, p. 541
 Hwang H. S. et al., 2010, *MNRAS*, 409, 75
 Ilbert O. et al., 2006, *A&A*, 457, 841
 Jarrett T. H. et al., 2011, *ApJ*, 735, 112
 Jarvis M. et al., 2016, Proc. Sci., The MeerKAT International GHz Tiered Extragalactic Exploration (MIGHTEE) Survey. SISSA, Trieste, PoS#6
 Johnston R., Vaccari M., Jarvis M., Smith M., Giovannoli E., Häußler B., Prescott M., 2015, *MNRAS*, 453, 2540
 Jonas J., MeerKAT Team, 2016, Proc. Sci., The MeerKAT Radio Telescope. SISSA, Trieste, PoS#1
 Kenyon J. S., Smirnov O. M., Grobler T. L., Perkins S. J., 2018, *MNRAS*, 478, 2399
 Klöckner H.-R., 2004, PhD thesis, Univ. Groningen
 Klöckner H.-R., Baan W. A., Garrett M. A., 2003, *Nature*, 421, 821
 Larson K. L. et al., 2016, *ApJ*, 825, 128
 Lo K. Y., 2005, *ARA&A*, 43, 625
 Lockett P., Elitzur M., 2008, *ApJ*, 677, 985
 Lonsdale C. J., Diamond P. J., Smith H. E., Lonsdale C. J., 1994, *Nature*, 370, 117
 McBride J., Heiles C., Elitzur M., 2013, *ApJ*, 774, 35
 Maddox N. et al., 2021, *A&A*, 646, A35
 Momjian E., Romney J. D., Carilli C. L., Troland T. H., 2006, *ApJ*, 653, 1172
 Norris R. P., Gardner F. F., Whiteoak J. B., Allen D. A., Roche P. F., 1989, *MNRAS*, 237, 673
 Offringa A. R. et al., 2014, *MNRAS*, 444, 606
 Perkins F., Gold T., Salpeter E. E., 1966, *ApJ*, 145, 361
 Pihlström Y. M., Baan W. A., Darling J., Klöckner H. R., 2005, *ApJ*, 618, 705
 Planck Collaboration VI, 2020, *A&A*, 641, A6
 Polatidis A. G., Aalto S., 2000, in Conway J. E., Polatidis A. G., Booth R. S., Pihlström Y. M. eds, EVN Symposium 2000, Proceedings of the 5th European VLBI Network Symposium., Onsala Space Observatory, p. 127
 Ponomareva A. A. et al., 2021, *MNRAS*, 508, 1195
 Ponomareva A. A. et al., 2023, *MNRAS*, 522, 5308
 Roberts H., Darling J., Baker A. J., 2021, *ApJ*, 911, 38
 Rovilos E., Diamond P. J., Lonsdale C. J., Lonsdale C. J., Smith H. E., 2003, *MNRAS*, 342, 373
 Rupke D. S., Veilleux S., Sanders D. B., 2005, *ApJS*, 160, 115
 Shirley R. et al., 2021, *MNRAS*, 507, 129
 Smith D. J. B. et al., 2013, *MNRAS*, 436, 2435
 Smith D. J. B. et al., 2014, *MNRAS*, 445, 2232
 Smolčić V. et al., 2017, *A&A*, 602, A1
 Spoon H. W. W. et al., 2013, *ApJ*, 775, 127
 Stalevski M., Fritz J., Baes M., Nakos T., Popović L. Č., 2012, *MNRAS*, 420, 2756
 Stalevski M., Ricci C., Ueda Y., Lira P., Fritz J., Baes M., 2016, *MNRAS*, 458, 2288
 Staveley-Smith L., Norris R. P., Chapman J. M., Allen D. A., Whiteoak J. B., Roy A. L., 1992, *MNRAS*, 258, 725
 Suess K. A., Darling J., Haynes M. P., Giovanelli R., 2016, *MNRAS*, 459, 220

Downloaded from https://academic.oup.com/mnras/article/529/4/3484/7473713 by guest on 11 July 2024

- Townsend R. H. D., Ivison R. J., Smail I., Blain A. W., Frayer D. T., 2001, *MNRAS*, 328, L17
- Tristram K. R. W., Scharfmann M., 2011, *A&A*, 531, A99
- Tristram K. R. W. et al., 2009, *A&A*, 502, 67
- Veilleux S., Kim D. C., Sanders D. B., 2002, *ApJS*, 143, 315
- Wang J. et al., 2023, *J. Astrophys. Astron.*, 44, 53
- Weaver H., Williams D. R. W., Dieter N. H., Lum W. T., 1965, *Nature*, 208, 29
- Weaver J. R. et al., 2022, *ApJS*, 258, 11
- Whitaker K. E. et al., 2014, *ApJ*, 795, 104
- Whittam I. H. et al., 2022, *MNRAS*, 516, 245
- Willett K. W., Darling J., Spoon H. W. W., Charmandaris V., Armus L., 2011a, *ApJS*, 193, 18
- Willett K. W., Darling J., Spoon H. W. W., Charmandaris V., Armus L., 2011b, *ApJ*, 730, 56
- Wilson W. J., Barrett A. H., 1968, *Science*, 161, 778
- Yuan T. T., Kewley L. J., Sanders D. B., 2010, *ApJ*, 709, 884
- Zhang J. S., Wang J. Z., Di G. X., Zhu Q. F., Guo Q., Wang J., 2014, *A&A*, 570, A110
- Zhu S., Brandt W. N., Zou F., Luo B., Ni Q., Xue Y., Yan W., 2023, *MNRAS*, 522, 3506
- Zou F. et al., 2022, *ApJS*, 262, 15
- ¹*Astrophysics, Department of Physics, University of Oxford, Keble Road, Oxford OX1 3RH, UK*
- ²*Department of Physics and Astronomy, University of the Western Cape, Robert Sobukwe Road, Bellville 7535, Cape Town, South Africa*
- ³*Department of Physics and Electronics, Rhodes University, PO Box 94, Makhanda 6140, South Africa*
- ⁴*South African Radio Astronomy Observatory, 2 Fir Street, Black River Park, Observatory, Cape Town 7925, South Africa*
- ⁵*Institute for Astronomy, Royal Observatory Edinburgh, Blackford Hill, Edinburgh EH9 3HJ, UK*
- ⁶*Wits Centre for Astrophysics, School of Physics, University of the Witwatersrand, 1 Jan Smuts Avenue, Johannesburg 2000, South Africa*
- ⁷*Department of Physics, University of Pretoria, Private Bag X20, Pretoria 0028, South Africa*
- ⁸*Max-Planck Institut für Radioastronomie, Auf dem Hügel 69, D-53121 Bonn, Germany*
- ⁹*School of Physics, H.H. Wills Physics Laboratory, Tyndall Avenue, University of Bristol, Bristol BS8 1TL, UK*
- ¹⁰*Department of Physics and Astronomy, Rutgers, The State University of New Jersey, 136 Frelinghuysen Road, Piscataway, NJ 08854-8019, USA*
- ¹¹*Department of Physics and Astronomy, Università degli Studi di Padova, Vicolo dell'Osservatorio 3, I-35122 Padova, Italy*
- ¹²*INAF – Osservatorio Astronomico di Padova, Vicolo dell'Osservatorio 5, I-35122 Padova, Italy*
- ¹³*Department of Space, Earth and Environment, Chalmers University of Technology, Onsala Space Observatory, SE-43992 Onsala, Sweden*
- ¹⁴*School of Physics and Astronomy, University of Minnesota, 116 Church St SE, Minneapolis, MN 55455, USA*
- ¹⁵*Minnesota Institute for Astrophysics, University of Minnesota, 116 Church St SE, Minneapolis, MN 55455, USA*
- ¹⁶*Cardiff Hub for Astrophysics Research & Technology, School of Physics & Astronomy, Cardiff University, Queens Buildings, The Parade, Cardiff CF24 3AA, UK*
- ¹⁷*Département d'Astronomie, Université de Genève, Chemin Pegasi 51, CH-1290 Versoix, Switzerland*
- ¹⁸*ASTRON, the Netherlands Institute for Radio Astronomy, Oude Hoogeveensedijk 4, NL-7991 PD Dwingeloo, the Netherlands*
- ¹⁹*Kapteyn Astronomical Institute, University of Groningen, PO Box 800, NL-9700 AV Groningen, the Netherlands*
- ²⁰*Sterrenkundig Observatorium, Universiteit Gent, Krijgslaan 281 S9, B-9000 Gent, Belgium*
- ²¹*National Radio Astronomy Observatory, 520 Edgemont Road, Charlottesville, VA 22903, USA*
- ²²*Inter-University Institute for Data Intensive Astronomy, Department of Astronomy, University of Cape Town, Rondebosch 7701, Cape Town, South Africa*
- ²³*Inter-University Institute for Data Intensive Astronomy, Department of Physics and Astronomy, University of the Western Cape, Bellville 7535, Cape Town, South Africa*
- ²⁴*INAF – Istituto di Radioastronomia, via Gobetti 101, I-40129 Bologna, Italy*

This paper has been typeset from a $\text{\TeX}/\text{\LaTeX}$ file prepared by the author.